On the Feasibility of a High-Sensitivity Imaging System for Biomedical Applications Based on Low-Frequency Magnetic Field

Sabrina Rotundo ⓘ , *Member, IEEE*, Danilo Brizi ⓘ , *Member, IEEE*, and Agostino Monorchio ⓘ , *Fellow, IEEE*

Abstract—In this article, the theoretical and experimental feasibility analyses of a high-sensitivity imaging system for non-invasive detection of pathological inclusions within biological tissues are presented. The radiating system, exploiting a low frequency magnetic field operating at 3 MHz, consists of an inner resonant spiral sensor, inductively coupled to an unloaded external planar probe loop. The proposed configuration produces a focused magnetic field distribution, therefore a high-sensitivity imaging with respect to the wavelength can be accomplished (detecting inclusions with size in the order of $\lambda/10000$, i.e., 1 cm). In particular, the inclusion detection is carried out by observing the amplitude shift of the external probe loop input impedance while scanning the region of interest, leading to a non-invasive and contactless imaging procedure. In addition, we demonstrate the possibility to detect an inclusion, placed within the investigated tissue, either with or without the use of a ferromagnetic contrast medium. To evaluate the proposed imaging system effectiveness, we first perform full-wave numerical simulations. Then, we report the experimental measurements acquired over a fabricated prototype interacting with a representative biological phantom, observing a very good agreement with the numerical simulations. The results confirm the potential for an innovative near-field imaging system to be employed for non-invasive detection of malignant inclusions, expanding the adoption of low RF frequencies in biomedical applications.

Index Terms—Biomedical applications, high sensitivity, imaging system, inductive methods, low frequency, resonant coil, sensor.

I. INTRODUCTION

RECENTLY, imaging systems are emerging as a very important research field, increasingly finding applications in different technological areas. Biomedical field is probably one of the most interesting, due to the huge impact of diagnostic imaging on the healthcare environment [1], [2], [3], [4], [5]. Beside traditional approaches, as Magnetic Resonance Imaging, X-rays tomography and ultrasound, novel imaging techniques based on the adoption of electromagnetic fields recently appeared in the literature [6]. The reasons for the diffusion of electromagnetic imaging systems rely on the reduced instrumentation complexity, minor side effects for patients and relatively lower costs that allow an easier and deeper adoption in healthcare facilities. Nevertheless, as any high-performing imaging device, they should allow an accurate, precise, and rapid diagnosis, therefore also optimizing the therapeutic procedure.

More specifically, among the various imaging solutions exploiting a radiofrequency magnetic field, magnetic particle imaging (MPI) raises as one of the most promising, providing high resolution and sensitivity by exploiting magnetic nanomaterials as contrast medium [7], [8], [9], [10], [11], [12]. In details, the contrast medium is placed in the target region directly *in situ* or through biological targeting mechanisms [13], [14].

The magnetic nanofluid reacts to the excitation field, producing a magnetization vector that contains the excitation frequency and also higher order harmonics due to non-linearities of its hysteresis cycle. By spatially selecting small regions to be excited with the RF magnetic field, it is possible to detect the higher order harmonics signal content and to finally reconstruct the image [15], [16]. Clearly, a crucial aspect is represented by the design of a radiating system able to produce a focused RF magnetic field distribution in a small portion of tissue, to progressively scan the entire volume of interest. This task is not trivial, since the adopted low frequencies are characterized by large wavelengths, making difficult the RF magnetic field focusing. A technical solution to face this issue is reported in [15]. The entire volume of interest is homogeneously exposed to a non-focused radio frequency magnetic field, superimposing a static magnetic field, characterized by a peculiar spatial distribution. Indeed, the static magnetic field, easier to be spatially shaped from a physical point of view, is absent only in a small region, from which the signal is collected. As a matter of fact, magnetic nanoparticles response to the RF excitation is suppressed if a sufficiently strong static field is superimposed. Then, this field-free region is progressively moved to cover the volume of interest and the nanoparticles localization is possible by observing the harmonics presence. Nevertheless, the required instrumentation is extremely complex [17]. Beside MPI, another promising contactless and non-invasive imaging technique exploiting an RF magnetic field is Magnetic Induction Tomography (MIT) [18], [19], [20], [21], [22]. By avoiding the use of any magnetic contrast medium, this method applies a radiofrequency magnetic field produced by an excitation coil to induce eddy currents in

the investigated tissue. Eddy currents arise because of the tissue dielectric properties, in particular the electrical conductivity. Generally, healthy and pathological tissues present different values of conductivity, mainly due to the water content, therefore generating a natural contrast [22], [23], [24]. The imaging is achieved by evaluating the magnetic field perturbation through an arrangement of receiving coils [21], [22], [23], [24], [25]. By measuring the induced secondary magnetic field, it is possible to have the inclusion spatial localization. A problematic aspect of MIT technique consists in the low resolution due to the weak signal of the secondary magnetic field. To improve this quantity, the imaging instrumentations have to include a higher receiving coils number, making the system more complex, bulky and expensive [26], [27], [28], [29].

To address the above-mentioned limits, we propose an innovative imaging system for contactless, high-sensitivity and non-invasive inclusions detection by using a low frequency magnetic field, operating at 3 MHz. This radiating element allows producing a focused magnetic field distribution, although the adopted low frequency. The most significant and innovative contributions, compared to traditional technologies, rely on the combination of low frequency, good sensitivity, and small dimensions, thus making the system safe, reliable, and portable. By monitoring the amplitude shift of the probe loop input impedance while scanning the investigated tissue, both in presence and in absence of a magnetic contrast medium, the imaging procedure can be accomplished. The object spatial localization is correlated to the magnetic field perturbation, due to the inclusion presence, that influences the system frequency response. In particular, the same exciting radiating element has also the function of receiver, significantly simplifying the required instrumentation.

The article is organized as follows. Section II describes the imaging system design and the physical model behind the inclusion detection, both with and without the use of a magnetic contrast medium. In Section III, the numerical and experimental test cases are reported while Section IV is devoted to present the numerical and experimental results. Finally, conclusions and future developments are discussed.

II. METHODS

A. Imaging System Design

Following the Introduction, the proposed radiating arrangement consists in an internal planar passive resonant coil, inductively coupled to an external, unloaded, concentric probe loop operating at 3 MHz [30], [31], [32]. The dual-spiral configuration has been adopted to avoid the power supply output impedance going in series with the sensing coil (thus, preserving its Q-factor) and, additionally, to guarantee more electrical safety. Therefore, the basic idea behind this configuration relies in creating a self-standing, resonating sensor, able to be extremely sensitive to changes in the electromagnetic properties of the surrounding medium. The external probe loop has the role to both feed the inner spiral sensor and to pick up the resulting impedance variations.
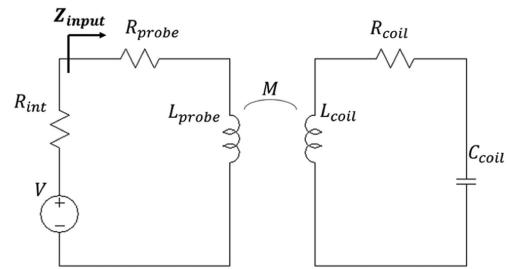

Fig. 1. Equivalent circuit of the proposed radiating configuration: the non-resonant probe is mutually coupled with the inner spiral resonator.

The operative frequency selection (3 MHz) is a trade-off between achieving a significant penetration depth inside tissues and obtaining an acceptable sensitivity. Moreover, the radiating system is designed to optimize the internal resonant coil Q-factor and, thus, the device sensitivity.

The imaging step is performed by placing the radiating system in proximity to the investigated object, and progressively carrying out a circular scanning around the volume of interest. Specifically, the spatial encoding of the target within the tissue is achieved by observing the variation of the external probe input impedance during the scan. Indeed, the target dielectric or magnetic contrast with respect to the surrounding tissues affects the magnetic field distribution and, consequently, the device input impedance. In this context, one of the more relevant advantages of the proposed system relies in the integration of the transmitting and receiving functions in one single device.

More quantitatively, the equivalent circuit of the described radiating configuration is depicted in Fig. 1. In the figure, R_{probe} and L_{probe} represent, respectively, the external probe loop resistance and inductance; R_{coil}, L_{coil} and C_{coil} indicate the internal spiral coil resistance, inductance and capacitance (the latter required for obtaining resonance). Finally, M denotes the inductive mutual coupling term between the probe and the coil. At this point, we can analytically express the probe loop input impedance Z_{input}:

$$Z_{input} = R_{probe} + j\omega L_{probe} + \frac{\omega^2 M^2}{R_{coil} + j\omega L_{coil} + \frac{1}{j\omega C_{coil}}}$$

(1)

In details, the useful signal for imaging is created by observing the maximum value of the probe input impedance, corresponding to the resonance frequency of the inner coil, for each scan angular position. Picking up the resonance point of the inner sensor allows exploiting the optimum sensitivity. Since the probe input impedance is dependent, in particular, on the electromagnetic properties of the surrounding biological medium (and also of the inclusion), the detection can be performed.

The aim of this work consists in the detection of a target placed inside the investigated tissue both with and without the use of a magnetic contrast medium; therefore, the next paragraphs are devoted to explaining the physical concepts behind the imaging procedure.

B. Case 1: Use of Magnetic Contrast Medium

As explained, a ferromagnetic medium can be an extremely effective way to increase the imaging performance in biomedical applications [33], [34], by realizing a high contrast with respect to biological tissues. Indeed, biological tissues are naturally non-magnetic, showing a relative permeability equal to 1. To implement a realistic scenario, the magnetic inclusion is simulated as a 10 mm diameter spherical geometry, with the typical electromagnetic properties of magnetite (Fe_3O_4) nanoparticles fluids [6], [11], [24], [25]. This spherical inclusion has been placed within the phantom, represented by a 100 mm diameter sphere of breast fat. As a matter of fact, the magnetic inclusion presence perturbs the magnetic field distribution by interacting with it. In particular, such interaction depends both on the target distance in relation to the radiative system and to its dimension. More specifically, the closer the inclusion to the radiating system, the stronger the effect on the magnetic field distribution. Similarly, larger inclusions are able to affect deeper the radiating system response.

One possibility to model the presence of the inclusion within the biological phantom is to adopt the mixing rules formulation to obtain an effective magnetic permeability which should be a function of the target position and size [35]. Therefore, the effective magnetic permeability can be expressed as:

$$\mu_{eff}(x,y,z) = \mu_{tissue} + 3\eta\mu_{tissue}$$
$$\times \frac{\mu_{inclusion} + \mu_{tissue}}{\mu_{inclusion} + 2\mu_{tissue} - \eta(x,y,z) \cdot (\mu_{inclusion} - \mu_{tissue})} \quad (2)$$

where μ_{tissue} indicates the investigated tissue permeability. Instead, $\mu_{inclusion}$ describes the inclusion complex magnetic permeability, estimated from the literature. Finally, the parameter η denotes the volumetric fraction between inclusion and tissue but weighted for the magnetic field spatial distribution produced by the radiating system. This weighting operation has the role to consider that the inclusion has an effect on the radiating system which is dependent from the spatial amplitude of the magnetic field. Therefore, η can be defined as:

$$\eta(x,y,z) = \frac{V_{inclusion} \cdot H(x,y,z)}{V_{field}} \quad (3)$$

For this reason, in (3), the term $H(x,y,z)$ corresponds to the normalized magnetic field point value within the region of interest. By referring to the specific set-up configuration, the radiating system senses the biological phantom presence in only one half space while free space is in the opposite half. Therefore, an equivalent system magnetic permeability μ_{equ} can be defined as:

$$\mu_{equ}(x,y,z) = \frac{\mu_{eff}(x,y,z) + 1}{2} \quad (4)$$

At this point, it is possible to introduce the retrieved equivalent permeability μ_{equ} inside the external probe input impedance expression, in particular affecting the inductance values (1). The final expression becomes:

$$Z_{input} = R_{probe} + j\omega L_{probe} \cdot \mu_{equ}(x,y,z)$$
$$+ \frac{\omega^2 M^2}{R_{coil} + j\omega L_{coil} \cdot \mu_{equ}(x,y,z) + \frac{1}{j\omega C_{coil}}} \quad (5)$$

To summarize, the inclusion providing a magnetic contrast is able to affect the input impedance of the radiating system external probe, correlated to the distance between the inclusion and the device. This is due to the higher amplitude of the magnetic field in proximity of the coils. In addition, a stronger impedance variation can be also obtained with a larger inclusion size. In both the cases, the equivalent permeability increases and, thus, the input impedance varies consequently.

C. Case 2: Natural Dielectric Contrast

Another physical modality to generate a variation in the external probe input impedance consists in exploiting a form of contrast directly coming from the natural properties of healthy and malignant tissues, due to the significantly different water content. In particular, considering a biological tissue, the dielectric permittivity can be expressed as a complex value (i.e., $\varepsilon' - j\varepsilon''$). The imaginary term refers to the losses happening inside the tissue, and it can be related to the electrical conductivity σ(S/m) by the following relationship:

$$\sigma = \omega\varepsilon_0\varepsilon'' \quad (6)$$

where $\varepsilon_0 = 8.85 \cdot 10^{-12}\frac{F}{m}$ is the vacuum dielectric permittivity and ω(rad/s) is the considered magnetic field pulsation.

Also in this scenario, we can define an equivalent complex permittivity, ε_{equ}, as the average of the two half-planes permittivity (one characterized by the tissue and inclusion presence, while the other with free space). Now, the variation is due to an effect on the capacitance term of the input impedance:

$$Z_{input} = Z_{probe} + \frac{\omega^2 M^2}{R_{coil} + j\omega L_{coil} + \frac{1}{j\omega\varepsilon_{equ}C_{coil}}} \quad (7)$$

Since the equivalent dielectric permittivity is a complex value, it is possible to explicitly report its contributions in the real and imaginary components.

$$\begin{cases} R_{equ} = R_{coil} + \frac{\varepsilon''_{equ}}{\omega C_{coil}\left(\varepsilon''^2_{equ} + \varepsilon'^2_{equ}\right)} \\ C_{equ} = C_{coil}\frac{\left(\varepsilon''^2_{equ} + \varepsilon'^2_{equ}\right)}{\varepsilon'_{equ}} \end{cases} \quad (8)$$

Hence, the probe input impedance can be expressed as:

$$Z_{input} = Z_{probe} + \frac{\omega^2 M^2}{R_{equ} + j\omega L_{coil} + \frac{1}{j\omega C_{equ}}} \quad (9)$$

where also the resistance term has been modified by the tissue presence. To conclude, as for the magnetic contrast, also the tissue dielectric properties variation influences the radiative system response. This allows, in principle, to detect and localize a dielectric inclusion inside the investigated tissue without recurring to a magnetic contrast medium.
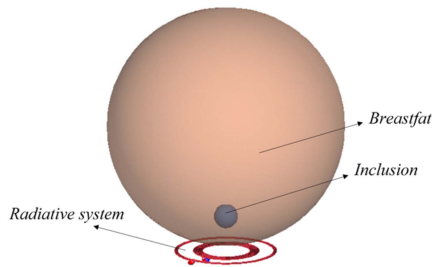
Fig. 2. CAD model of the proposed experimental set-up. The inclusion represents the pathological region inside the investigated tissue.

Fig. 3. Fabricated prototype. (a) Upper view; (b) bottom view.

TABLE I
IMAGING SYSTEM RF COILS GEOMETRICAL PROPERTIES

	N	External radius (mm)	Internal radius (mm)	Wire radius
Internal coil	8	20	16	AWG 28
External probe	3	10	8.5	AWG 28

TABLE III
MAGNETIC AND GEOMETRICAL PROPERTIES OF THE FERRITE ROD USED AS FERROMAGNETIC CONTRAST MEDIUM

	Diameter (mm)	Length (mm)	A_e (mm²)	μ_i	μ_{eff} @3MHz
Ferrite rod	6.35	25	7.07	29	125

TABLE II
MAGNETIC AND DIELECTRIC PROPERTIES OF THE ADOPTED BREAST TISSUE WITH AND WITHOUT MAGNETIC NANOPARTICLES' FLUID (MNF)

	ε_r	σ ($\frac{S}{m}$)	ρ ($\frac{kg}{mm^3}$)	μ_r'	$\tan\delta$ ($\frac{\mu_r''}{\mu_r'}$)
Breast Tissue	14.2	0.026	1200	1	-
Tumoral Inclusion	69	0.75	1200	1	-
Tumoral Inclusion with MNF	69	0.75	1200	1.67	0.413

III. NUMERICAL AND EXPERIMENTAL TEST-CASE

A. Numerical Test-Case

In order to demonstrate the validity of the described theory, we conceived a numerical test-case, exploiting an electromagnetic solver based on the Method of Moments (Feko Suite, Altair, Troy, MI, USA).

Firstly, we designed the radiating system adopting 3 MHz as operating frequency. Both the external and internal coils were made with a 28 AWG single strand lossy copper wire. The corresponding CAD is reported in Fig. 2, while Table I summarizes the geometrical features of the RF coils. The inner coil was made resonant at the operative frequency by adding an opportune tuning capacitor of 1.10 nF, thus achieving a Q-factor equal to 130. Beside the radiating system, we also designed a spherical biological phantom to realistically simulate the investigated tissue (specifically, a human breast). The phantom diameter has been selected as 100 mm while its dielectric properties, reported in Table II, are representative of the human breast at 3 MHz [23]. Since the imaging procedure is envisioned to be contactless, the biological phantom was placed 2 mm above from the radiating system (Fig. 2). To evaluate
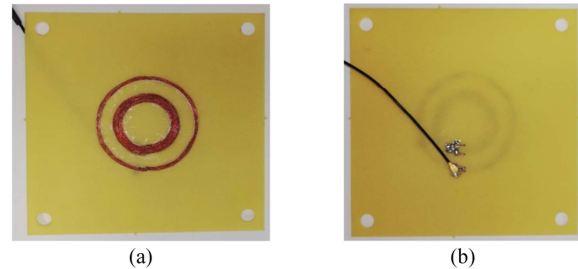
the inclusion detection capability, we recreated the pathological target by realizing a 10 mm diameter sphere, placed inside the tissue (Fig. 2). In the first configuration, we assumed that the inclusion contains also magnetite nanoparticles fluids, whose electromagnetic properties are reported in the literature and in Table II ([33], [34]). In the second test-case, we considered a purely dielectric inclusion with the electromagnetic properties of a pathological breast tissue region ("Tumoral Inclusion" in Table II). All the other parameters (radiating system, phantom size) remained unchanged with respect to the first scenario.

B. Experimental Test-Case: Fabricated Prototype

Beside numerical simulations, we fabricated prototypes of the proposed configurations to experimentally validate the imaging system performance. To reduce the ohmic losses with respect to adopting copper traces etched with PCB technology, we used a 0.8 mm thick FR4 slab ($\varepsilon_r = 4.3$ and $\tan\delta = 0.025$) as supporting substrate over which 28 AWG single strand copper wire was glued following the spiral coils patterns (Fig. 3) [36]. On the bottom, we equipped the external probe coil with a 50-Ω-micro-SMA connector to enable measurements with a vector network analyzer (Fieldfox series VNA N9918A, Keysight, Santa Rosa, CA, USA), while the internal coil was made resonant by soldering a 1.10 nF capacitor. The biological phantom was realized by employing agar (E406) at 2% w/v in water, inside a cylindrical glass container having a diameter of 100 mm and a height of 150 mm. The phantom was placed 2 mm away from the radiating system, as specified in the numerical model. With regard to the target inclusion, due to the difficulty to find commercial availability for nanoparticles fluids, we emulated the ferromagnetic contrast medium by inserting within the phantom a small ferrite rod, which properties are reported in Table III. Clearly, the contrast produced by the ferrite is much larger than what a magnetic nanoparticles fluid can achieve; nevertheless, the physical mechanism of interaction with the RF magnetic field is the same in this frequency band. In the second experimental
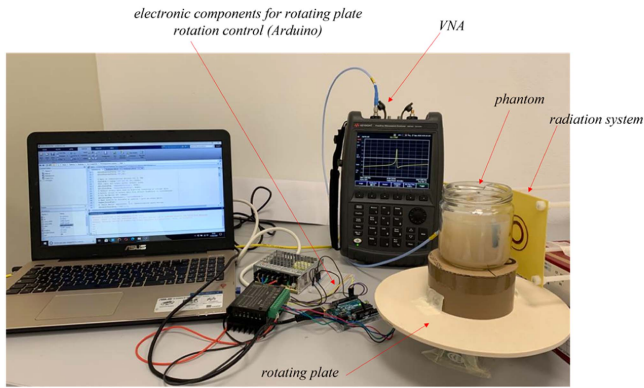
Fig. 4.   Complete experimental set-up.

configuration, we evaluated the system capability to detect a purely dielectric inclusion. In this case, we realized a dielectric sphere (diameter equal to 10 mm) using agar at 5% w/v in water. In addition, to simulate the different conductivity between healthy and pathological region, we added 6% w/v of NaCl. To perform a circular scanning, the phantom is positioned on a rotating platform, controlled by a stepper motor (NEMA17 Bipolar Stepper Motor). The stepper motor is driven by a microcontroller (Arduino UNO board). Finally, VNA acquisition and platform rotation are synchronized through a code developed in Matlab. The whole acquisition system is reported in Fig. 4.

IV. NUMERICAL AND EXPERIMENTAL RESULTS

In this section, we reported the imaging results of numerical simulations and experimental measurements by following the previously described procedure. In particular, the external probe loop impedance acquisition has been carried out with an angular step of $d\vartheta = 1^0$, both in simulation and in measurement, placing the biological phantom with the inclusions presence over the rotating platform at 2 mm from the radiating system. In order to validate the described physical imaging mechanism, we performed circular scans with the magnetic/dielectric inclusions at different radial distances from the radiating system (i.e., at different depths within the phantom). During this scan, the external probe loop impedance value corresponding to the resonance frequency of the inner spiral (3 MHz, see (1)) was registered. Specifically, Fig. 5(a) shows the amplitude of the full-wave signals during a circular scan when the nanoparticles' fluid inclusion (Table II) is placed 1.5 and 3.5 cm far from the radiating system, respectively (i.e., progressively deeper in the phantom). In particular, the signal has been normalized by subtracting the minimum impedance value obtained during the scan to the other angular positions. Therefore, in Fig. 5(a) the maximum impedance variation corresponds to the angular position in which the radiating system and the inclusion are aligned (at 0° in this case); indeed, in that position, the inclusion influence on the equivalent medium experienced by the radiating system is maximum, as theoretically predicted (1). Beside the angular position, the magnetic inclusion contribution to the input

impedance at 3 MHz is also basically related to the exciting magnetic field amplitude, as also expected. The field intensity rapidly decreases with the distance between the radiating system and the phantom. Indeed, at 1.5 cm, the maximum impedance variation is around 45.23 Ω. At 3.5 cm, this value drops at 0.54 Ω. Therefore, it is also possible to correlate the target inclusion depth with the impedance maximum variation. Beside numerical simulations, we reproduced the same configuration through our experimental set-up; Fig. 5(b) reports the measured signals in presence of the agar phantom with the ferrite inclusion (μ_{eff} at 3MHz equal to 125) for the same two distances (i.e., 1.5 and 3.5 cm). As a general observation, the experimental results are in excellent agreement with the simulations; the differences on the signal values can be imputed to the intrinsic differences between the numerical and the experimental phantoms. After having validated the imaging for a magnetic inclusion, the same procedure has been applied to the dielectric target immersed within the phantom (Table II). In Fig. 5(c), the obtained numerical results have been reported for two distances between the target and the radiating system, i.e., 5 mm and 10 mm, respectively. The smaller distances with respect to the magnetic inclusion are due to the inferior contrast produced by the dielectric target, which limits the useful imaging range. In particular, we observed a maximum input impedance variation of 2.4 Ω and 1.9 Ω for the two positions, respectively. As before, the angle position of the minimum of the impedance graph is related to the angle position of the target (in this case −40°), whereas the signal variation is correlated to the inclusion depth. We then compared the simulation results about the dielectric inclusion case against experimental measurements. Fig. 5(d) shows the results where an overall good agreement with the numerical simulations can be appreciated. Nevertheless, also in this second inclusion case, the experimental results present an amplitude smaller than the simulation, again due to the different phantom properties and unavoidable experimental noise. Finally, by starting from these preliminary scenarios, we also faced the issue to create a bi-dimensional image. In order to accomplish this task, we noticed that the signal obtained from a single circular scan closely resembles a typical signal obtained with a X-rays tomographic scanner [37], [38]. Therefore, we applied the algorithm of back projection to a data set. In particular, the signals showed in Fig. 5 are related to one sensor rotating around the phantom. To have a complete sinogram, N linear sensor for each angular position have to be employed (Fig. 6(a)-(b)). Backed by the good agreement between numerical and experimental results, we simulated a linear array of 9 sensors rotating around the phantom, in which we placed a magnetic inclusion. To evaluate the capability of the approach to achieve accurate spatial information, we acquired two images with different target position inside the phantom. The obtained 2D images are reported in Fig. 6(c)-(d), where both the dimension and the position of the inclusion are satisfactorily reconstructed. Finally, the metric employed to evaluate the quality of the reconstructed 2D images with respect to the ground truth consists in the percentage Mean Squared Error (MSE) calculation, resulting equal to an average value of 4.12%.
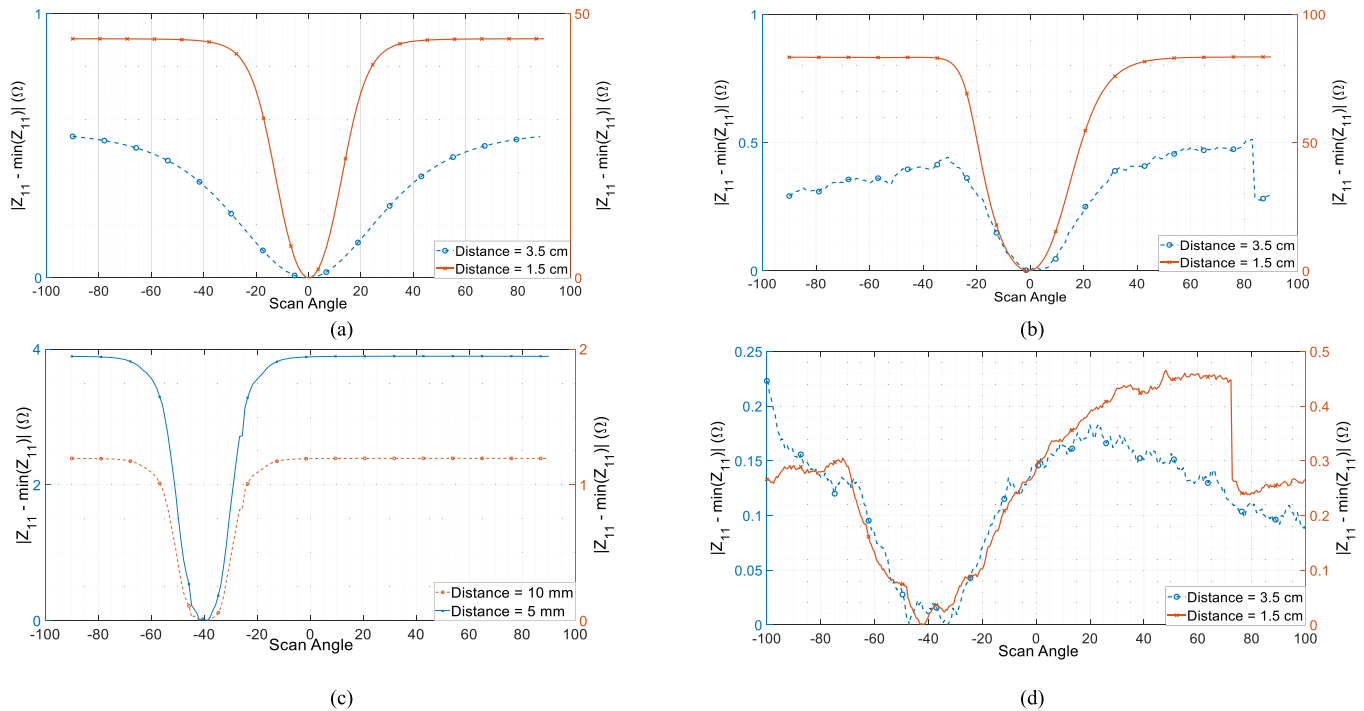
Fig. 5. Numerical (a) and experimental (b) results of the imaging procedure single scan with the magnetic inclusion placed at 1.5 cm and 3.5cm far from the radiating system. The normalized signals are obtained by subtracting the minimum value registered during the scan. Numeric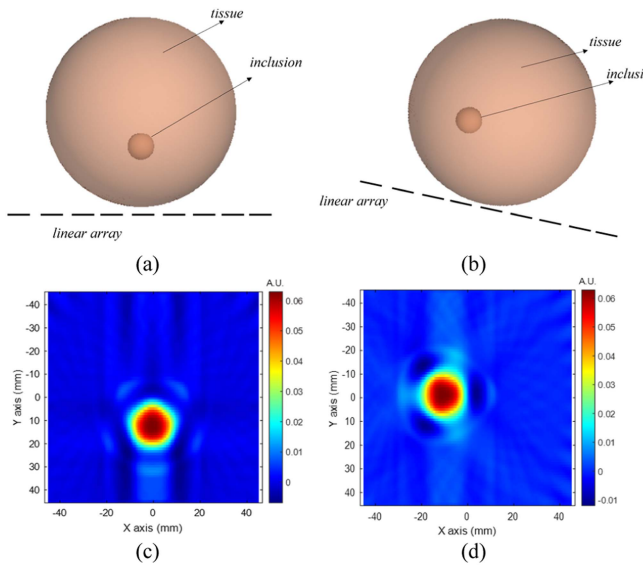al (c) and experimental (d) results of the imaging procedure single scan with the dielectric inclusion placed at 5 mm and 10 mm far from the radiating system. Again, the normalized signals are obtained by subtracting the minimum value registered during the scan.

Fig. 6. (a)—(b) CAD model representing a linear array; (c)—(d) numerically obtained 2D image applying the back projection imaging algorithm.

V. CONCLUSION

In this article, the theorical and experimental feasibility analyses of a hand-held and high-sensitivity imaging system exploiting a low-frequency magnetic field and suited for non-invasive pathological inclusion detection have been presented. In particular, the hardware configuration consists of a resonant spiral coil inductively coupled to an unloaded concentric planar probe loop able to produce a focused field distribution, even at low frequency (3 MHz). By developing an opportune circuital model, we conceived the possibility to detect an inclusion both with a magnetic or a naturally dielectric contrast. In order to verify the circuital model, we designed a radiating system, performing accurate numerical simulations on biological phantoms with dielectric and magnetic inclusions. After that, we also fabricated an experimental set-up of the radiating system and of the signal acquisition chain, achieving an excellent agreement with the simulations. The obtained spatial sensitivity (around 10 mm, $\lambda/10000$) is extremely satisfying, considering that the operating wavelength is extremely large at 3 MHz. Finally, we proved the possibility to reconstruct 2D images adopting a back projection algorithm, increasing the flexibility of the procedure. To conclude, these results reveal promising and future works will be directed to further optimize the radiating system performance.

REFERENCES

[1] H. Song, H. Sato, X. Xiao, and T. Kikkawa, "A portable breast cancer imaging system with cross-shaped dome antenna array," in *Proc. IEEE 11th Eur. Conf. Antennas Propag.*, 2017, pp. 3474–3475, doi: 10.23919/EuCAP.2017.7928284.

[2] L. Almenar et al., "Utility of cardiac magnetic resonance imaging for the diagnosis of heart transplant rejection," *Transplant. Proc.*, vol. 35, no. 5, pp. 1962–1964, Aug. 2003, doi: 10.1016/S0041-1345(03)00653-5.

[3] E. Mikhaylova et al., "Prototype small-animal PET-CT imaging system for image-guided radiation therapy," *IEEE Access*, vol. 7, pp. 143207–143216, 2019, doi: 10.1109/ACCESS.2019.2944683.

[4] X. Zhang, M. S. Noor, C. B. McCracken, Z. H. T. Kiss, O. Yadid-Pecht, and K. Murari, "CMOS image sensor and system for imaging hemodynamic changes in response to deep brain stimulation," *IEEE Trans. Biomed. Circuits Syst.*, vol. 10, no. 3, pp. 632–642, Jun. 2016, doi: 10.1109/TBCAS.2015.2453256.

[5] S. Rotundo, D. Brizi, A. Flori, G. Giovannetti, L. Menichetti, and A. Monorchio, "Shaping and focusing magnetic field in the human body: State-of-the art and promising technologies," *Sensors*, vol. 22, no. 14, Jul. 2022, Art. no. 5132, doi: 10.3390/s22145132.

[6] R. M. Ferguson, A. P. Khandhar, and K. M. Krishnan, "Tracer design for magnetic particle imaging (invited)," *J. Appl. Phys.*, vol. 111, no. 7, Apr. 2012, Art. no. 07B318, doi: 10.1063/1.3676053.

[7] S. Herz et al., "Magnetic particle imaging for quantification of vascular stenoses: A phantom study," *IEEE Trans. Med. Imag.*, vol. 37, no. 1, pp. 61–67, Jan. 2018, doi: 10.1109/TMI.2017.2717958.

[8] D. Brizi et al., "A novel approach for determining the electromagnetic properties of a colloidal fluid with magnetic nanoparticles for hyperthermia applications," *IEEE J. Electromagn., RF Microw. Med. Biol.*, vol. 2, no. 1, pp. 70–77, Mar. 2018, doi: 10.1109/JERM.2018.2799992.

[9] R. M. Ferguson, K. R. Minard, and K. M. Krishnan, "Optimization of nanoparticle core size for magnetic particle imaging," *J. Magnetism Magn. Mater.*, vol. 321, no. 10, pp. 1548–1551, May 2009, doi: 10.1016/j.jmmm.2009.02.083.

[10] K. Murase et al., "Usefulness of magnetic particle imaging for predicting the therapeutic effect of magnetic hyperthermia," *Open J. Med. Imag.*, vol. 05, no. 02, pp. 85–99, 2015, doi: 10.4236/ojmi.2015.52013.

[11] R. E. Rosensweig, "Heating magnetic fluid with alternating magnetic field," *J. Magnetism Magn. Mater.*, vol. 252, pp. 370–374, Nov. 2002, doi: 10.1016/S0304-8853(02)00706-0.

[12] D. Brizi et al., "A radiating system for low-frequency highly focused hyperthermia with magnetic nanoparticles," *IEEE J. Electromagn., RF Microw. Med. Biol.*, vol. 4, no. 2, pp. 109–116, Jun. 2020, doi: 10.1109/JERM.2019.2945833.

[13] R. Bazak, M. Houri, S. E. Achy, W. Hussein, and T. Refaat, "Passive targeting of nanoparticles to cancer: A comprehensive review of the literature," *Mol. Clin. Oncol.*, vol. 2, no. 6, pp. 904–908, Nov. 2014, doi: 10.3892/mco.2014.356.

[14] T. D. Clemons, R. Singh, A. Sorolla, N. Chaudhari, A. Hubbard, and K. S. Iyer, "Distinction between active and passive targeting of nanoparticles dictate their overall therapeutic efficacy," *Langmuir*, vol. 34, no. 50, pp. 15343–15349, Dec. 2018, doi: 10.1021/acs.langmuir.8b02946.

[15] B. Gleich and J. Weizenecker, "Tomographic imaging using the nonlinear response of magnetic particles," *Nature*, vol. 435, no. 7046, pp. 1214–1217, Jun. 2005, doi: 10.1038/nature03808.

[16] P. W. Goodwill and S. M. Conolly, "The X-space formulation of the magnetic particle imaging process: 1-D signal, resolution, bandwidth, SNR, SAR, and magnetostimulation," *IEEE Trans. Med. Imag.*, vol. 29, no. 11, pp. 1851–1859, Nov. 2010, doi: 10.1109/TMI.2010.2052284.

[17] T. F. Sattel, O. Woywode, J. Weizenecker, J. Rahmer, B. Gleich, and J. Borgert, "Setup and validation of an MPI signal chain for a drive field frequency of 150 kHz," *IEEE Trans. Magn.*, vol. 51, no. 2, Feb. 2015, Art. no. 6501703, doi: 10.1109/TMAG.2014.2326256.

[18] Z. Zakaria et al., "Advancements in transmitters and sensors for biological tissue imaging in magnetic induction tomography," *Sensors*, vol. 12, no. 6, pp. 7126–7156, May 2012, doi: 10.3390/s120607126.

[19] Y. Chen et al., "Imaging hemorrhagic stroke with magnetic induction tomography: Realistic simulation and evaluation," *Physiol. Meas.*, vol. 31, no. 6, pp. 809–827, Jun. 2010, doi: 10.1088/0967-3334/31/6/006.

[20] N. G. Gencer and M. N. Tek, "Electrical conductivity imaging via contactless measurements," *IEEE Trans. Med. Imag.*, vol. 18, no. 7, pp. 617–627, Jul. 1999, doi: 10.1109/42.790461.

[21] A. Korjenevsky, V. Cherepenin, and S. Sapetsky, "Magnetic induction tomography: Experimental realization," *Physiol. Meas.*, vol. 21, no. 1, pp. 89–94, Feb. 2000, doi: 10.1088/0967-3334/21/1/311.

[22] C. Tan, Y. Wu, Z. Xiao, and F. Dong, "Optimization of dual frequency-difference MIT sensor array based on sensitivity and resolution analysis," *IEEE Access*, vol. 6, pp. 34911–34920, 2018, doi: 10.1109/ACCESS.2018.2849412.

[23] S. Gabriel, R. W. Lau, and C. Gabriel, "The dielectric properties of biological tissues: III. Parametric models for the dielectric spectrum of tissues," *Phys. Med. Biol.*, vol. 41, no. 11, 1996, Art. no. 2271.

[24] A. Martellosio et al., "Dielectric properties characterization from 0.5 to 50 GHz of breast cancer tissues," *IEEE Trans. Microw. Theory Techn.*, vol. 65, no. 3, pp. 998–1011, Mar. 2017, doi: 10.1109/TMTT.2016.2631162.

[25] B. J. Mohammed, M. Manoufali, S. A. R. Naqvi, K. S. Bialkowski, P. C. Mills, and A. M. Abbosh, "Using dielectric properties of solid fraction and water content to characterize tissues at different health and age conditions," *IEEE J. Electromagn., RF Microw. Med. Biol.*, vol. 4, no. 1, pp. 69–77, Mar. 2020, doi: 10.1109/JERM.2019.2952054.

[26] M. S. Badri Mansor et al., "Magnetic induction tomography: A brief review," *J. Teknol*, vol. 73, no. 3, pp. 91–95, Mar. 2015, doi: 10.11113/jt.v73.4252.

[27] H. Y. Wei and M. Soleimani, "Electromagnetic tomography for medical and industrial applications: Challenges and opportunities [point of view]," *Proc. IEEE*, vol. 101, no. 3, pp. 559–565, Mar. 2013, doi: 10.1109/JPROC.2012.2237072.

[28] K. Stawicki, S. Gratkowski, M. Komorowski, and T. Pietrusewicz, "A new transducer for magnetic induction tomography," *IEEE Trans. Magn.*, vol. 45, no. 3, pp. 1832–1835, Mar. 2009, doi: 10.1109/TMAG.2009.2012799.

[29] Q. Du, B. Bai, L. Ke, and X. Lin, "Design of sector multi-channel detecting system for magnetic induction tomography," in *Proc. IEEE Int. Conf. Comput. Appl. Syst. Model.*, 2010, pp. V4–129–V4–132, doi: 10.1109/ICCASM.2010.5619311.

[30] D. Brizi, J. P. Stang, A. Monorchio, and G. Lazzi, "On the design of planar arrays of nonresonant coils for tunable wireless power transfer applications," *IEEE Trans. Microw. Theory Techn.*, vol. 68, no. 9, pp. 3814–3822, Sep. 2020.

[31] S. Rotundo, D. Brizi, and A. Monorchio, "A feasibility study of a low-frequency wearable device for contactless monitoring of blood glucose level," in *Proc. IEEE Int. Symp. Antennas Propag. USNC-URSI Radio Sci. Meeting*, 2021, pp. 367–368, doi: 10.1109/APS/URSI47566.2021.9704100.

[32] S. Rotundo, D. Brizi, and A. Monorchio, "A feasibility study of a radio-frequency theranostic device for tumor localization and treatment," in *Proc. IEEE 16th Eur. Conf. Antennas Propag.*, 2022, pp. 1–4, doi: 10.23919/EuCAP53622.2022.9769397.

[33] P. A. Dresco, V. S. Zaitsev, R. J. Gambino, and B. Chu, "Preparation and properties of magnetite and polymer magnetite nanoparticles," *Langmuir*, vol. 15, no. 6, pp. 1945–1951, Mar. 1999, doi: 10.1021/la980971g.

[34] Z. R. Stephen, F. M. Kievit, and M. Zhang, "Magnetite nanoparticles for medical MR imaging," *Mater. Today*, vol. 14, no. 7–8, pp. 330–338, Jul. 2011, doi: 10.1016/S1369-7021(11)70163-8.

[35] A. Sihvola, "Mixing rules with complex dielectric coefficients," *Subsurface Sens. Technol. Appl.*, vol. 1, no. 4, pp. 393–415, 2000.

[36] G. Giovannetti, G. Tiberi, M. Tosetti, A. Monorchio, and N. Fontana, "Radiofrequency planar surface coil for magnetic resonance: When the use of a circular wire gives a noticeable advantage with respect to a flat strip conductor?," *Measurement*, vol. 129, pp. 518–522, Dec. 2018, doi: 10.1016/j.measurement.2018.07.060.

[37] B. J. Darrer, J. C. Watson, P. Bartlett, and F. Renzoni, "Toward an automated setup for magnetic induction tomography," *IEEE Trans. Magn.*, vol. 51, no. 1, Jan. 2015, Art. no. 6500104, doi: 10.1109/TMAG.2014.2355420.

[38] A. V. Korjenevsky and S. A. Sapetsky, "Feasibility of the backprojection method for reconstruction of low contrast perturbations in a conducting background in magnetic induction tomography," *Physiol. Meas.*, vol. 38, no. 6, pp. 1204–1213, Jun. 2017, doi: 10.1088/1361-6579/aa6605.

Sabrina Rotundo (Student Member, IEEE) was born in Bari, Italy, in 1993. She received the M.Sc. degree in biomedical engineering from the University of Pisa, Pisa, Italy, in 2020. She is currently working toward the Ph.D. degree with the Department of Information Engineering. Since January 2023, she has been a Visiting Research Scholar with NYU Langone, New York, NY, USA. Her research interests include electromagnetic metasurfaces, MRI hardware system, and RF sensors for theranostic applications.

Danilo Brizi (Member, IEEE) was born in Viterbo, Italy, in 1992. He received the M.Sc. degree (*summa cum laude*) in biomedical engineering and the Ph.D. degree (*summa cum laude*) in information engineering from the University of Pisa, Pisa, Italy, in 2016 and 2020, respectively. From 2018 to 2019, he was Visiting Research Scholar with the Keck School of Medicine, University of Southern California, Los Angeles, CA, USA. He is currently an Assistant Professor with the University of Pisa. In 2023, he was selected among the top reviewers of the IEEE TRANSACTIONS ON ANTENNAS AND PROPAGATION. His research interests include electromagnetic metasurfaces, MRI filter design, and wireless power transfer applications. He was also the recipient of the young Scientist Award of the URSI-GASS International Symposium on Electromagnetic Theory, URSI General Assembly in 2020. Since 2022, he has been an Associate Editor for the *IEEE Antennas and Propagation Magazine*.

Agostino Monorchio (Fellow, IEEE) is currently a Full Professor with the University of Pisa, Pisa, Italy. He has carried out a considerable research activity and technical consultancy to national, EU and U.S. industries, coordinating, as principal scientific investigator, a large number of national and European research projects. He is a Reviewer for international journals, and he was an Associate Editor for IEEE ANTENNAS AND WIRELESS PROPAGATION LETTERS from 2002 to 2007.

He is active in a number of areas including computational electromagnetics, microwave metamaterials, radio propagation for wireless systems, the design and miniaturization of antennas and electromagnetic compatibility, biomedical applications of RF and microwaves.

The activity is mainly carried out with the Microwave and Radiation Laboratory, Department of Information Engineering, University of Pisa, together with a large group of Ph.D. students, Postdocs and Research Associates. He is the Head of RaSS National Laboratory of CNIT (Consorzio Nazionale Interuniversitario per le Telecomunicazioni). He is a Member of the Scientific Advisory Board of Directed Energy Research Center of TII, Abu Dhabi, UAE, and affiliated with the Pisa Section of INFN, the National Institute of Nuclear Physics. His research results have been authored or coauthored in more than 170 journal papers and book chapters, and more than 260 communications at international and national conferences, he is the co-author of four patents. He spent several research periods with the Electromagnetic Communication Laboratory, Pennsylvania State University, State College, PA, USA, as the recipient of a scholarship (Fellowship Award) of the Summa Foundation, New Mexico (USA), and in the framework of CNR-NATO Senior Fellowship Programme. In 2012, he has been elevated to Fellow grade by the IEEE for his contributions to computational electromagnetics and for application of frequency selective surfaces in metamaterials.